

Broadband multi-region sound insulator by utilizing quasi-Sierpinski carpet structure

Saeed Aliakbarzadeh and Ali Bahrami

Citation: Chin. Phys. B, 2026, 35 (**6**): 064302. DOI: 10.1088/1674-1056/ae063a
http://cpb.iphy.ac.cn; http://iopscience.iop.org/cpb

What follows is a list of articles you may be interested in

Ultrasonic scalpel based on fusiform phononic crystal structure

Sha Wang(王莎), Junjie Shan(单俊杰), and Shuyu Lin(林书玉)
Chin. Phys. B, 2024, 33 (**10**): 104302. DOI: 10.1088/1674-1056/ad6a0c

Inverse design of nonlinear phononic crystal configurations based on multi-label classification learning neural networks

Kunqi Huang(黄坤琦), Yiran Lin(林懿然), Yun Lai(赖耘), and Xiaozhou Liu(刘晓宙)
Chin. Phys. B, 2024, 33 (**10**): 104301. DOI: 10.1088/1674-1056/ad6b85

Sensing the heavy water concentration in an H_2O—D_2O mixture by solid—solid phononic crystals

Mohammadreza Rahimi and Ali Bahrami
Chin. Phys. B, 2024, 33 (**4**): 044301. DOI: 10.1088/1674-1056/ad0bf5

Nonlinear wave propagation in acoustic metamaterials with bilinear nonlinearity

Shiqi Liang(梁诗琪), Jiehui Liu(刘杰惠), Yun Lai(赖耘), and Xiaozhou Liu(刘晓宙)
Chin. Phys. B, 2023, 32 (**4**): 044301. DOI: 10.1088/1674-1056/ac9783

Tunable topological interface states and resonance states of surface waves based on the shape memory alloy

Shao-Yong Huo(霍绍勇), Long-Chao Yao(姚龙超), Kuan-Hong Hsieh(谢冠宏), Chun-Ming Fu(符纯明), Shih-Chia Chiu(邱士嘉), Xiao-Chao Gong(龚小超), and Jian Deng(邓健)
Chin. Phys. B, 2023, 32 (**3**): 034303. DOI: 10.1088/1674-1056/ac8727

Broadband multi-region sound insulator by utilizing quasi-Sierpinski carpet structure

Saeed Aliakbarzadeh and Ali Bahrami†

Optoelectronics and Nanophotonics Research Laboratory (ONRL), Faculty of Electrical Engineering, Sahand University of Technology, Tabriz, Iran

(Received 21 July 2025; revised manuscript received 11 September 2025; accepted manuscript online 12 September 2025)

The effects of rotation, size, and geometric shape of rods within a quasi-Sierpinski carpet fractal structure on bandgap behavior were investigated. In the first stage of the Sierpinski carpet ($L = 1$), rotating the central rod from 0° to 45° led to a slight increase in the bandgap width at frequencies between 0 kHz and 5 kHz. In the second stage ($L = 2$), rotating the side rods gradually expanded the bandgap width, increasing it from approximately 2.7 kHz to over 3.3 kHz. Although the bandgaps in the third stage ($L = 3$) were narrower compared to those in the previous two stages, new bandgaps appeared at frequencies between 16 kHz and 20 kHz. Varying the size of the central rod from $a/27$ to $a/2$ led to an overall increase in the bandgap size from 1 kHz to 3.65 kHz. Geometric modifications also played a significant role in bandgap size; for instance, the use of a dodecagonal central rod generated the widest bandgap of 3.42 kHz, while the combination of a diamond-shaped central rod with circular side rods resulted in a bandgap size of 2.19 kHz. The results indicate that such modifications can significantly optimize the bandgaps in terms of both frequency position and width. These findings can contribute to the design of advanced materials for applications such as acoustic insulation, vibration reduction, and mechanical wave control.

Keywords: phononic crystals, bandgaps, Sierpinski carpet, fractal

PACS: 43.20.+g, 43.55.Ti, 43.35.Gk, 05.45.Df

DOI: 10.1088/1674-1056/ae063a **CSTR:** 32038.14.CPB.ae063a

1. Introduction

Phononic crystals (PnCs) are artificial periodic structures formed by repeating rods within a matrix.[1,2] PnCs can be classified as solid–solid, solid–fluid, or fluid–fluid structures. The repetition of rods within the matrix can be one-dimensional, two-dimensional, or three-dimensional, leading to the creation of one-dimensional (1D), two-dimensional (2D), and three-dimensional (3D) PnCs. The most prominent feature of PnCs is their band gaps, where frequencies within these ranges cannot pass through the structure. The ability to control and engineer acoustic and elastic waves using PnCs-based components is a primary reason for the growing interest in these structures in recent years. Some of the applications of PnCs include noise control,[3] vibration reduction,[4] seismic control,[5] sound insulation,[6] energy harvesting,[7] and switching.[8]

The main focus in PnCs is to adjust the band gaps, and fractal structures like the Sierpinski carpet, due to their self-similar geometry and a high effective surface area, can enhance the performance of PnC.[9] One of the key characteristics of fractal structures is the creation of multiple band gaps as the stage increases, without altering the unit cell size.[10,11]

Huang *et al.* investigated the Sierpinski carpet structure in terms of band gaps and wave propagation characteristics.[11] Their findings indicated that only the second iteration of the structure exhibited a relatively suitable band gap.[9] To enhance the filling fraction and significantly adjust the PnC dispersion relation, modifications were introduced to the Sierpinski carpet, leading to the development of two novel quasi-Sierpinski carpet structures. In these modified structures, the size of the central rod was increased, which resulted in wider band gaps and a greater number of band gaps compared to the conventional Sierpinski carpet. Ozer *et al.* explored the impact of quasi-fractal designs on the band structures of PnC to achieve large band gaps.[12] They proposed two distinct quasi-Sierpinski unit cells, which were composed of four different materials. The band gaps for these structures were reported as 10.79 kHz and 18.47 kHz. However, the primary challenge with these configurations was the complexity of integrating four different materials within the structure. Johanson *et al.* designed Sierpinski carpet structures with circular rods, consisting of an epoxy substrate embedded with steel cylinders coated by silicone rings. Despite their innovative design, these structures faced difficulties in assembling three different materials together and exhibited relatively narrow band gaps.[2]

Beyond Sierpinski carpet-based structures, other studies have shown that fractal geometries can play a significant role in enhancing band gaps. Norris *et al.*[13] demonstrated that fractal structures in phononic crystals can create band gaps at low frequencies due to local resonance. Wen *et al.*[14] also investigated porous quasi-fractal structures with a Sierpinski triangle pattern and observed that increasing the fractal order

†Corresponding author. E-mail: bahrami@sut.ac.ir

© 2026 Chinese Physical Society and IOP Publishing Ltd. All rights, including for text and data mining, AI training, and similar technologies, are reserved.

leads to multiple and wider band gaps. Liu and Fan[15] studied T-square-type fractal structures and reported that fractal repetition significantly alters the dispersion relations and highlights the importance of rod geometry in controlling wave propagation.

In addition to rod geometry, the angle and rotation of the rods play a crucial role in the formation of band gaps. Vasseur *et al.*[16] demonstrated that rotating square rods in a periodic array alters the unit cell symmetry, which can either increase or decrease the band gap width depending on the rotation angle. Oltulu *et al.*[17] investigated the rotation of elliptical rods in two-dimensional (2D) phononic crystal arrays and showed that such rotations can modify the band gap widths, with these changes being dependent on the unit cell symmetry.

Overall, the review of these studies indicates that both fractal organization and rod geometry modification are two key approaches for designing phononic crystals with wider and more tunable band gaps. In this paper, the effect of rotating rods by 0°, 15°, 30°, and 45° at different stages of the Sierpinski carpet, the size variation of the central rod, and the geometric deformation of the rods on the scattering curve and band gap are investigated. By selecting optimal configurations, particularly at the second stage of the Sierpinski carpet, the band gap can be effectively expanded and shifted toward desired frequencies.

The rest of this paper is organized as follows: Section 2 presents the fundamental concepts. Section 3 presents the design and simulation of the Sierpinski carpet structure at different stages, along with the corresponding dispersion curves.

2. Theoretical background

The Sierpinski carpet is one of the most well-known fractal structures, discovered by Wacław Sierpinski in 1916.[12] This structure follows a recursive pattern. Figure 1 shows the Sierpinski carpet structure at the first, second, and third stages, respectively.

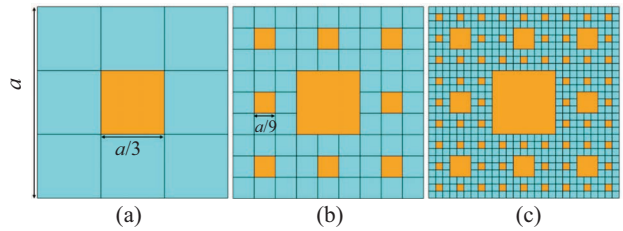


Fig. 1. Sierpinski carpet unit cell at different stages, $K = 1$ and $M = 3$: (a) $L = 1$, $N = 9$; (b) $L = 2$, $N = 81$; (c) $L = 3$, $N = 729$.

To design a Sierpinski carpet, first, a square unit cell with lattice constant $a = 1.5$ mm is divided into nine equal squares. Then, the material of the central square is replaced, forming the first stage of the Sierpinski carpet. This process is repeated for the remaining eight squares to obtain the second stage. The third stage is created in the same manner. The number of squares at each stage is obtained using the equation $N = M^{2L}$, where L is the Sierpinski carpet stage and M is the number of initial lattice cells along the x or y axis. With each stage of the Sierpinski carpet, the filling fraction increases, which can be calculated using[9]

$$f = \frac{\sum_{i=1}^{L} 8^{(L-i)}\left(K^2 M^{2(i-1)}\right)}{M^{2L}}. \tag{1}$$

In this equation, K represents the number of orange squares in the x and y directions. The central position of each square is calculated using[2,9]

$$r_i = r_b + \frac{a}{M^L}(s-1), \quad s = 1, \ldots, KM^{L-1}. \tag{2}$$

such that $i = x, y$ and it is also obtained from[2,9]

$$r_b = \begin{cases} \dfrac{a(1-KM^{L-1})}{2M^L}, & s = 1, \ldots, (KM^{L-1}-1), \\ \dfrac{a(KM^{L-1}-1)}{2M^L}, & s = KM^{L-1}. \end{cases} \tag{3}$$

In this structure, lead is chosen as the rod material for the orange parts, and rubber is selected as the substrate material for the blue parts. The elastic parameters of these materials are shown in Table 1.

Table 1. Constituent materials and elastic parameters.

Material	Poisson's ratio	Young's modulus (GPa)	Mass density (kg/m^3)
Rubber	0.4688	1.175×10^{-4}	1300
Pb	0.3968	40.819	11600

Considering that both the substrate and the rod are solid, the fundamental equations for modeling elastic wave propagation in solid–solid phononic crystals, as well as for designing unit cell configurations to achieve desired bandgap properties, are presented as follows:

$$T_{ij}(\boldsymbol{r},t) = c_{ijkl}(\boldsymbol{r})\, u_{k,l}(\boldsymbol{r},t), \tag{4}$$

$$T_{ij}(\boldsymbol{r},t) = \rho(\boldsymbol{r})\frac{\partial^2 u_i(\boldsymbol{r},t)}{\partial t^2}. \tag{5}$$

In these equations, T_{ij} and u_i represent the stress tensor and displacement in the three spatial directions, respectively. Additionally, c_{ijkl} and ρ denote the elastic constants and the mass density. By combining Eqs. (4) and (5), we obtain

$$\left(c_{ijkl}(\boldsymbol{r})\, u_{k,l}(\boldsymbol{r},t)\right)_{,j} = \rho(\boldsymbol{r})\frac{\partial^2 u_i(\boldsymbol{r},t)}{\partial t^2}. \tag{6}$$

Equation (6) is considered the primary relation for modeling solid–solid phononic crystals. By eliminating the stress tensor and applying the Bloch–Floquet theorem, these relations provide a theoretical framework that allows precise prediction of bandgap formation, serving as a guiding tool for the design and analysis of solid–solid phononic crystal structures.

3. Design and simulations

In this section, Sierpinski carpet structures are simulated at different stages. Figure 2 shows the Sierpinski carpet structure at stage $L = 1$ with rod rotation, along with the corresponding dispersion curves.

As shown in Fig. 2, in the Sierpinski carpet structure at stage $L = 1$, a band gap is formed in the low-frequency range with a value of approximately 0.27 kHz in the non-rotated case (0°), which is represented in blue. With the increase in the central rod rotation angle, the size of this band gap increases and reaches 0.32 kHz at a 45° rotation. No band gaps are observed at medium and higher frequencies. Overall, the results indicate that applying rotation to the central rod in the first-stage Sierpinski carpet structure is an effective method for slightly enhancing the band gap at low frequencies; however, this approach shows limited effectiveness in generating band gaps at higher frequencies.

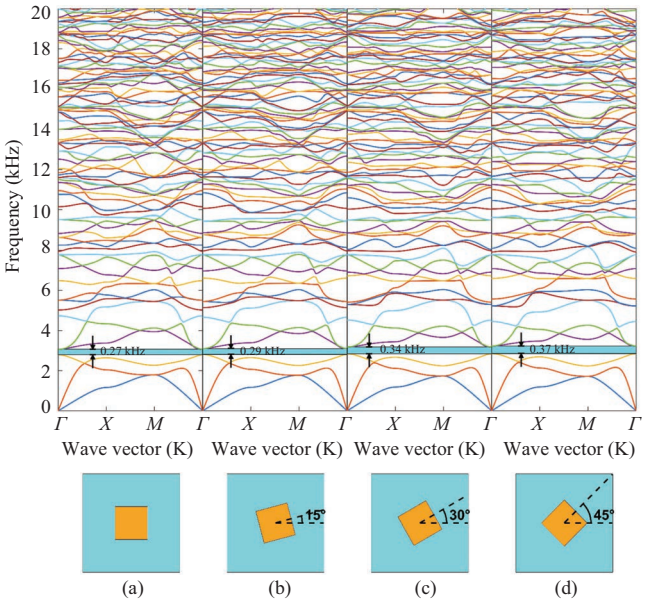


Fig. 2. The dispersion curve of the Sierpinski carpet unit cell at $L = 1$ with central rod rotations of (a) 0°, (b) 15°, (c) 30°, and (d) 45°.

Upon transitioning from stage $L = 1$ to $L = 2$, changes are observed in the structure's results, including the dispersion curve. Figure 3 shows the Sierpinski carpet structure at stage $L = 2$, where the rotated side rods are depicted along with the corresponding dispersion curves for each case.

According to Fig. 3, by rotating the side rods at angles of 0°, 15°, 30°, and 45°, the bandgap in the low-frequency range observed in Fig. 2 disappears, and several bandgaps appear in the mid-frequency range. Additionally, multiple bandgaps are created in the higher-frequency range. At medium and high frequencies, the bandwidth of the bandgaps increases with the rotation of the rods. When the side rods are rotated by 45°, a narrow bandgap of 0.18 kHz appears at 19 kHz, which did not exist in the previous structures. Overall, the bandwidths of the bandgaps for structures with side rod rotations of 0°, 15°, 30°, and 45° are 2.58, 2.83, 3.11, and 3.18 kHz, respectively. These results indicate that rotating the central rod in the second-stage Sierpinski carpet structure is more suitable for adjusting the bandgap in the mid-frequency range rather than at other frequencies.

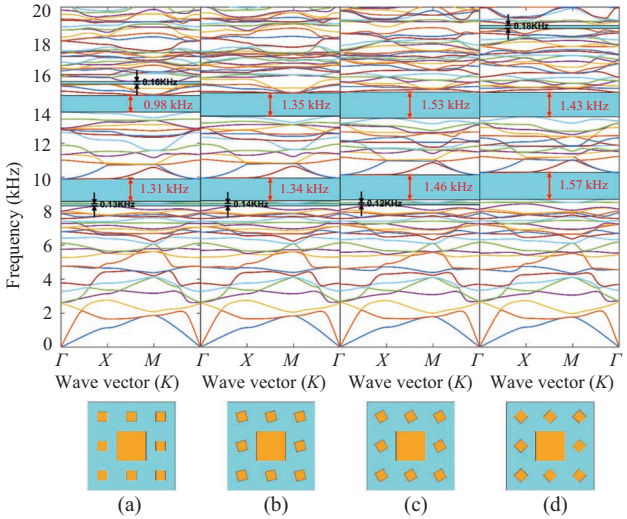


Fig. 3. The dispersion curve of the Sierpinski carpet unit cell at $L = 2$ with side rotations of (a) 0°, (b) 15°, (c) 30°, and (d) 45°.

When transitioning from stage $L = 2$ to $L = 3$, changes in the structure's results, including the dispersion curve, are observed. Figure 4 shows the Sierpinski carpet structure at stage $L = 3$, with the smallest rotated rods and their corresponding dispersion curves.

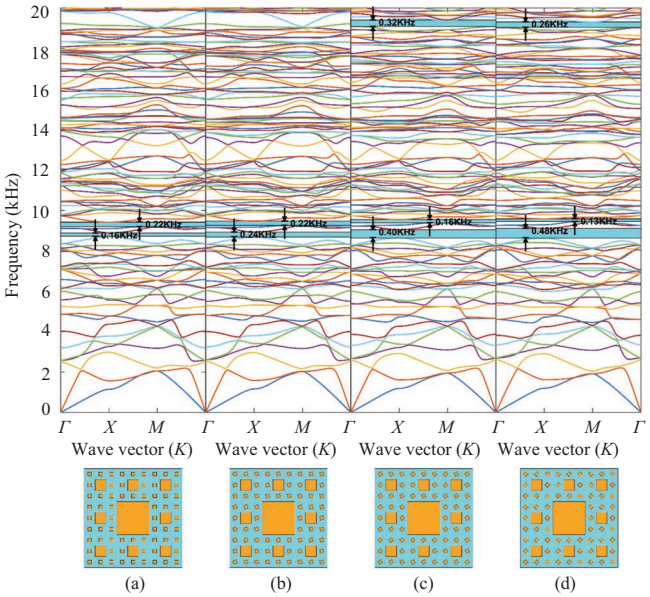


Fig. 4. The dispersion curve of the Sierpinski carpet unit cell at $L = 3$ with rotations of the smallest rods at (a) 0°, (b) 15°, (c) 30°, and (d) 45°.

According to Fig. 4, which shows the rotation of the smallest rods at angles of 0°, 15°, 30°, and 45°, the bandgap in the low-frequency range observed in Fig. 2 no longer exists. Bandgaps appear in the mid-frequency range and are considerably smaller than those observed in Fig. 3. In this structure, with rotations of 30° and 45°, a narrow bandgap at 19 kHz is created, which previously existed only in the $L = 2$ structure

with a 5° rotation and was narrower than these two bandgaps. The overall bandwidths of the bandgaps for the smallest rods at rotation angles of 0°, 15°, 30°, and 45° are 0.38, 0.46, 0.88, and 0.87 kHz, respectively, which are significantly smaller compared to those of the second-stage Sierpinski carpet structure.

In general, the Sierpinski carpet structure $L = 1$ is more suitable for creating band gaps in the lower frequency range, while $L = 2$ is more appropriate for creating band gaps in the medium frequency range. Because the bandgap size in the $L = 2$ stage is larger than those in the other two stages, this stage has been examined more thoroughly in the following analysis. Figure 5 shows the Sierpinski carpet structure at $L = 2$, where the central rod is rotated by 15° and the side rods are rotated by 0°, 15°, 30°, and 45°, along with their corresponding dispersion curves.

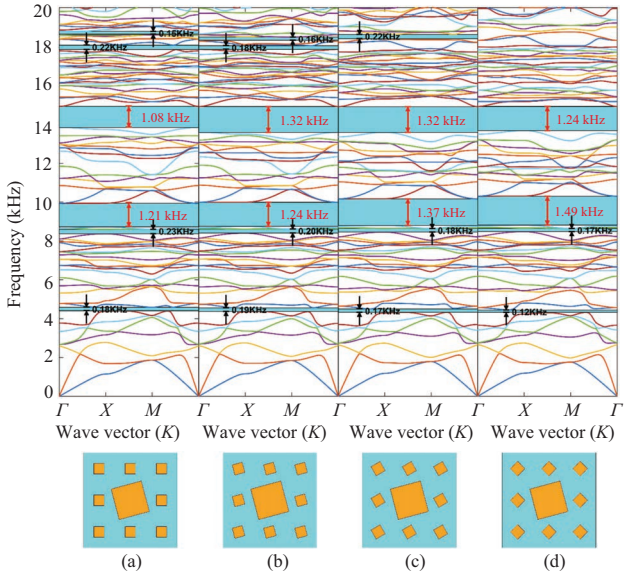


Fig. 5. The dispersion curve of the Sierpinski carpet unit cell at $L = 2$ with a 15° rotation of the central rod and rotations of the side rods at (a) 0°, (b) 15°, (c) 30°, and (d) 45°.

According to Fig. 5, which shows the Sierpinski carpet structure at $L = 2$ with a 15° rotation of the central rod and rotations of the side rods, a band gap is created in the lower frequency range, which was not present in Fig. 3. As the rotation of the side rods increases, the band gap width in the lower frequency range decreases, and the widths of two band gaps in the higher frequency range also reduce. In the range of 8 kHz to 10 kHz, two band gaps appear, and with increasing rotation of the side rods, the upper band gap becomes wider while the lower band gap becomes narrower. Additionally, in the range of 13 kHz to 15 kHz, two band gaps are present, and as the rotation of the side rods increases, the upper band gap widens while the lower band gap becomes narrower, eventually disappearing at a 45° rotation. Overall, in this figure, the total number of band gaps in the range of 0 kHz to 20 kHz increases as the rotation of the side rods increases, with their total sizes for rotations of 0°, 15°, 30°, and 45° being 3.07, 3.29, 3.26, and 3.02, respectively.

By changing the rotation of the central rod from 15° to 30°, variations in the dispersion curve of the structure are observed. Figure 6 shows the Sierpinski carpet structure at $L = 2$, with the central rod rotated by 30° and the side rods rotated by 0°, 15°, 30°, and 45°, along with their corresponding dispersion curves.

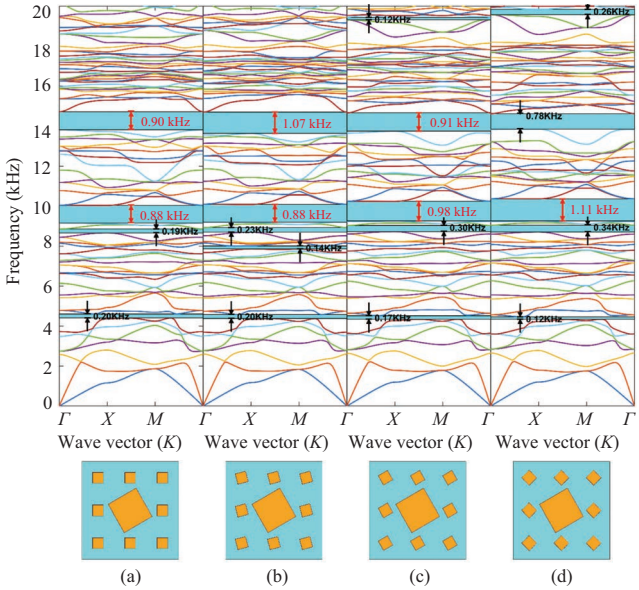


Fig. 6. The dispersion curve of the Sierpinski carpet unit cell at $L = 2$ with a 30° rotation of the central rod and rotations of the side rods at (a) 0°, (b) 15°, (c) 30°, and (d) 45°.

According to Fig. 6, where the central rod is rotated by 30° and the side rods are rotated by 0°, 15°, 30°, and 45°, the 30° rotation of the central rod results in a decrease in the overall band gap size compared to Fig. 5. Additionally, as the rotation of the side rods increases, the number of band gaps in the lower frequency range increases, but the width of the band gap that existed in the non-rotated case has decreased. In the medium frequency range, some of the band gaps have disappeared with increasing rotation, but the widths of the three main band gaps have increased. In the higher frequency range, a narrow band gap has appeared with increasing rotation.

When the rotation of the central rod changes from 30° to 45°, variations in the structure's dispersion curve are observed. Figure 7 shows the Sierpinski carpet structure at $L = 2$, with the central rod rotated by 45° and the side rods rotated by 0°, 15°, 30°, and 45°, along with their corresponding dispersion curves.

In Fig. 7, as the rotation of the side rods increases, the band gap size in the 10-kHz range has increased, while the band gap in the 14-kHz range has decreased. In the lower frequency range, several narrow band gaps have appeared with increasing rotation of the side rods. At the 45° rotation of the side rods, a band gap appears in the approximately 20-kHz range. Overall, the band gap sizes for rotations of 0°, 15°,

30°, and 45° are 1.55, 1.68, 1.70, and 1.77 kHz, respectively. According to the results obtained from the rotation of the rods, rod rotation has a significant effect on the band gap, which occurs through several physical mechanisms. First, rotating the rods alters the geometric symmetry of the structure, and this change in symmetry modifies the wave propagation paths and their interference conditions. Second, rod rotation changes the local resonance frequencies, thereby tuning the position and width of the band gap.

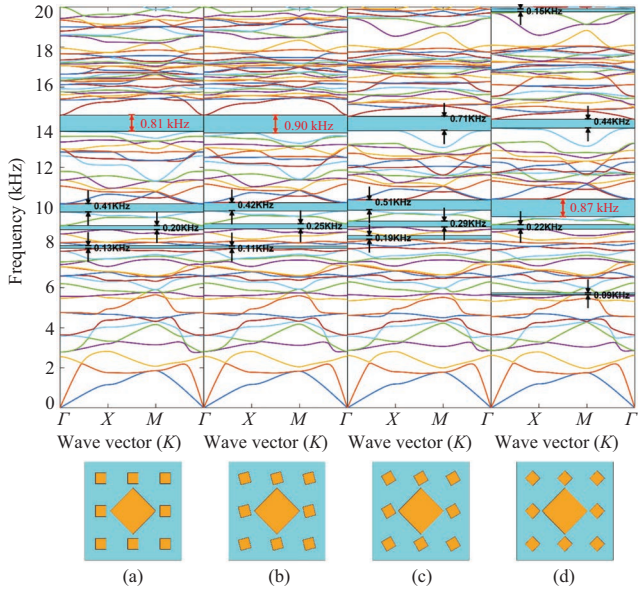


Fig. 7. The dispersion curve of the Sierpinski carpet unit cell at $L = 2$ with a 45° rotation of the central rod and rotations of the side rods at (a) 0°, (b) 15°, (c) 30°, and (d) 45°.

In the next step, the effects of changing the size of the central rod on the band gaps in the Sierpinski carpet structure at $L = 2$ were examined, and the structure and its corresponding dispersion curve are shown in Fig. 8.

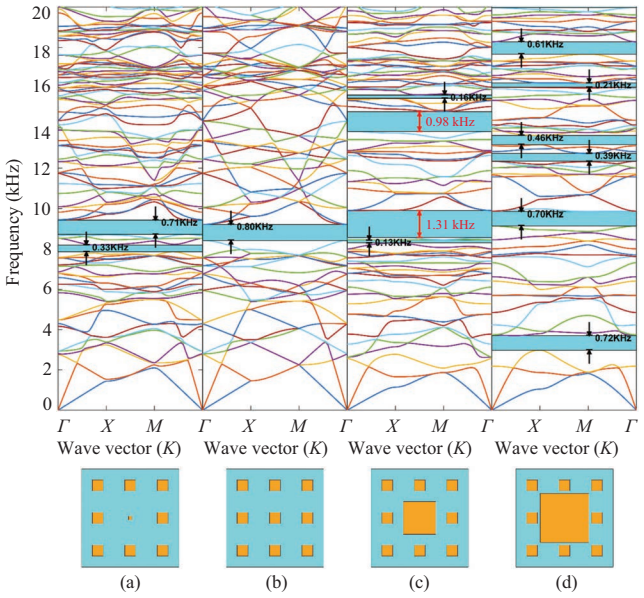


Fig. 8. The dispersion curve of the Sierpinski carpet unit cell at $L = 2$ with the central rod sizes of (a) $a/27$, (b) $a/9$, (c) $a/3$, and (d) $a/2$.

According to the results presented in Fig. 8, it can be observed that increasing the size of the central rod increases both the number and size of the band gaps. In the first two cases, band gaps are only present in the frequency range between 8 kHz and 10 kHz, whereas in the third case, band gaps also appear in higher frequency ranges. In the final case, in addition to the increased number of band gaps in the medium and high frequency ranges, a band gap also appears in the lower frequency range. The total band gap sizes for the Sierpinski carpet structure with small to large central rods are 1.04 kHz, 0.80 kHz, 2.58 kHz, and 3.09 kHz, respectively. Increasing the dimensions of the rods affects both the position and width of the band gaps and enhances the scattering and local resonance mechanisms. As the rods become larger, the wave interference conditions and Bragg scattering are altered, and the local resonance frequencies are modified; this leads to an expansion of the band gap and an increase in the frequency range through which acoustic waves cannot propagate. Furthermore, the band gap size also increases from the first to the fourth case, which is attributed to the increase in the filling fraction.

In the next step, the effects of a 45° rotation of the central rod and its size variation on the band gaps in the Sierpinski carpet structure at $L = 2$ were examined, and the results are shown in Fig. 9.

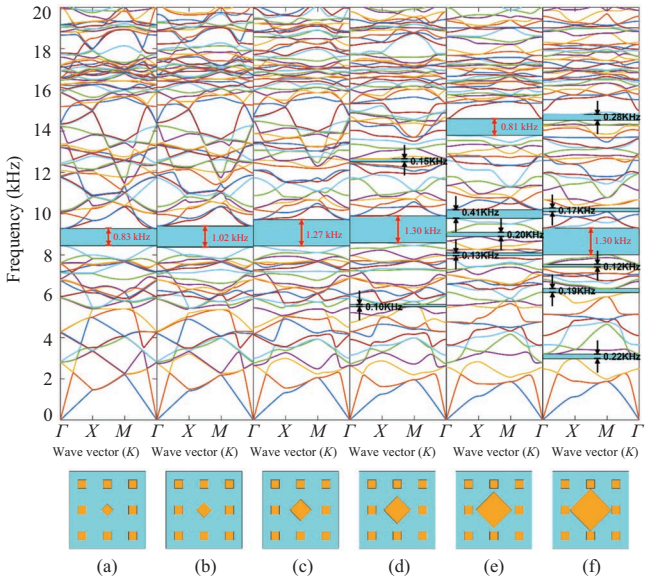


Fig. 9. The dispersion curve of the Sierpinski carpet unit cell at $L = 2$, with the central rod rotated by 45° and its size set to (a) $a/9$, (b) $a/7$, (c) $a/5$, (d) $a/4$, (e) $a/3$, and (f) $3a/8$.

According to the results presented in Fig. 9, as the size of the central rod increases, both the number and width of the band gaps increase. The total band gap sizes for the central rod from smallest to largest are 0.83 kHz, 1.02 kHz, 1.27 kHz, 1.55 kHz, 1.55 kHz, and 2.28 kHz, respectively. The structure with a larger central rod exhibits the highest number of band gaps and is the only structure that has a band gap in the lower frequency range. The band gap in the lower frequency range

for the structure with a larger central rod in Fig. 9 is narrower compared to the corresponding structure in Fig. 8. However, the band gap in the medium frequency range is wider. In terms of overall band gap size, the structure in Fig. 9 has fewer band gaps compared to the structure in Fig. 8. Moreover, this increase in bandgap sizes, similar to the structures in Fig. 8, is due to the increase in the filling fraction.

Next, the effect of changing the geometry of the central rod on the band gaps in the Sierpinski carpet structure at $L = 2$ is investigated, and the results are shown in Fig. 10.

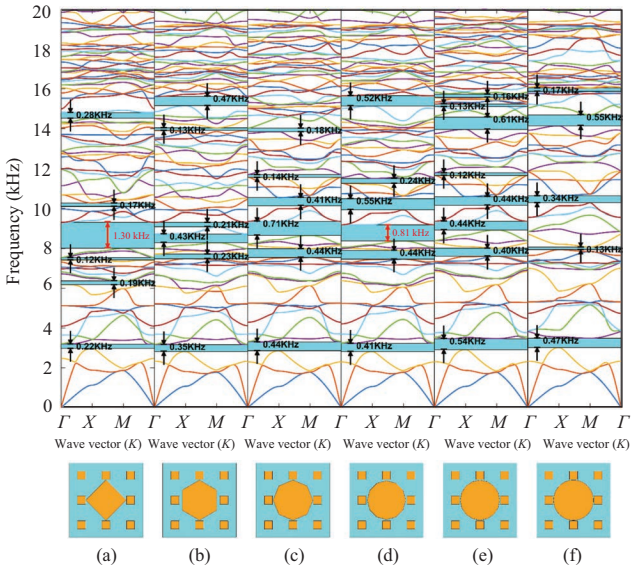


Fig. 10. The dispersion curve of the Sierpinski carpet unit cell at $L = 2$, where the shape of the central rod is (a) rhombus, (b) hexagon, (c) octagon, (d) dodecagon, (e) hexadecagon, and (f) circle.

In Fig. 10, different geometric shapes of the central rod are shown from left to right in the following order: rhombus, hexagon, octagon, dodecagon, hexadecagon, and circle. The band gap in the lower frequencies increases with shape variation, reaching its maximum when the central rod is a hexadecagon. In the medium frequency range, the structure with a rhombus-shaped rod has the widest band gap. However, as the central rod shape changes to a circle, this band gap disappears, while in other cases, it splits into several narrower band gaps. Among these, the dodecagon exhibits the largest band gap in this range. At frequencies between 14 kHz and 20 kHz, the hexadecagon has the widest and most prominent band gap compared to the other structures. The total band gap sizes for the structures in Fig. 10, from left to right, are 2.28 kHz, 1.82 kHz, 2.32 kHz, 2.97 kHz, 2.84 kHz, and 1.66 kHz, with the largest values observed for the dodecagon and hexadecagon. According to the results, the geometric shape has a direct impact on the band gaps, such that angular shapes (*e.g.*, the dodecagon) produce wider band gaps, whereas round shapes (*e.g.*, the circle) result in narrower band gaps. This is due to differences in local resonance and Bragg scattering. Additionally, the smaller band gap of the rhombus compared to other polygons is attributed to its lower filling fraction.

After analyzing the effect of changing the central rod geometry on the band gap, the influence of modifying the geometry of the side rods in the Sierpinski carpet structure at $L = 2$, with a rhombus-shaped central rod, is examined. The results are presented in Fig. 11.

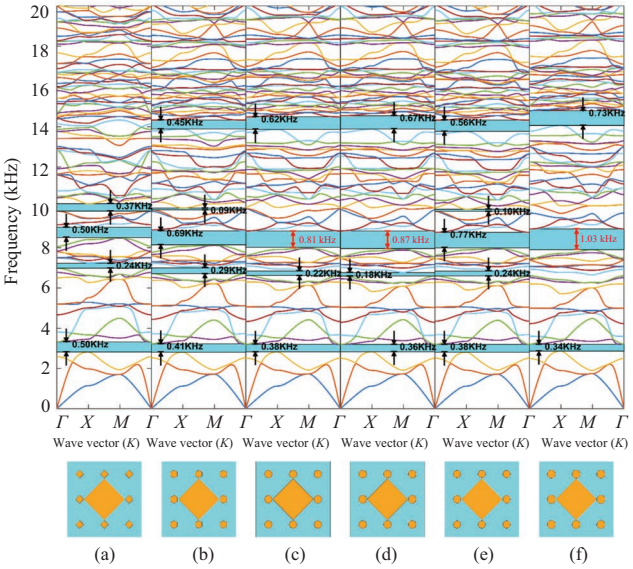


Fig. 11. Dispersion curve of the unit cell of the Sierpinski carpet at $L = 2$, where the central rod is rhombus-shaped, and the side rods are, respectively: (a) rhombus, (b) hexagon, (c) octagon, (d) dodecagon, (e) hexadecagon, and (f) circle.

In Fig. 11, different shapes of the side rods are shown from left to right in the following order: rhombus, hexagon, octagon, dodecagon, hexadecagon, and circle, while the central rod remains rhombus-shaped. At lower frequencies, the band gap size decreases as the shape of the side rods changes from a rhombus to a circle. In the medium frequency range, when the side rods are rhombus-shaped, three band gaps are present. As the shape of the side rods changes, the middle band gap widens, while the other two gradually become narrower. At 14 kHz, when the side rods are rhombus-shaped, a very narrow band gap of approximately 0.001 kHz exists. However, as the shape of the side rods changes, this band gap widens, reaching 0.73 kHz when the side rods are circular. The total band gap sizes for the side rods in the shapes of a rhombus, hexagon, octagon, dodecagon, hexadecagon, and circle are 1.61 kHz, 1.93 kHz, 2.03 kHz, 2.08 kHz, 2.05 kHz, and 2.1 kHz, respectively.

Next, the effect of changing the geometry of the central rod on the band gap in the Sierpinski carpet structure at $L = 2$, with circular side rods, is examined. The results are presented in Fig. 12.

As shown in Fig. 12, by changing the shape of the central rod from rhombus to circle, the band gap at lower frequencies increases. For the structure with a circular central rod, the band gap at low frequencies reaches 0.64 kHz. At 14 kHz, the width of the band gap decreases as the central rod shape changes from rhombus to circle. Additionally, the band gap

present in the rhombus-shaped central rod splits into two narrower band gaps. At medium frequencies, when the central rod is rhombus-shaped, a single wide band gap exists. However, as the central rod shape changes, the number of band gaps increases, while their widths decrease. The total band gap sizes for the structure with circular side rods and central rods in the shapes of rhombus, hexagon, octagon, dodecagon, hexadecagon, and circle are 2.1 kHz, 2.54 kHz, 2.14 kHz, 2.75 kHz, 2.31 kHz, and 1.86 kHz, respectively.

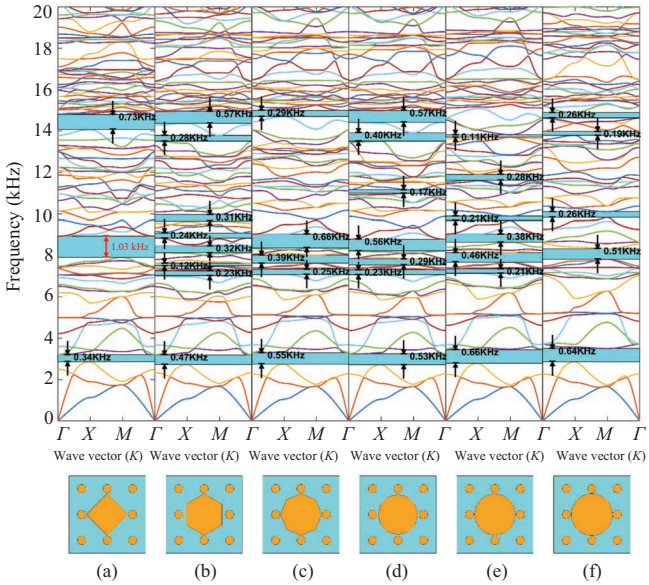


Fig. 12. Scattering curve of the unit cell of the Sierpinski carpet at $L = 2$, where the side rods are circular, and the central rod shapes are: (a) rhombus, (b) hexagon, (c) octagon, (d) dodecagon, (e) hexadecagon, and (f) circle.

4. Discussion

The structures presented in this study each possess specific characteristics tailored to different applications. To identify optimal configurations, we considered both the width of the bandgap and the frequency range in which the bandgaps occur. Based on these criteria, the second-stage ($L = 2$) structure with a square central rod of size $a/2$ exhibits superior performance, as it provides the widest bandgap among the investigated designs. Furthermore, the second-stage ($L = 2$) structure with a dodecagonal central rod and square side rods can be regarded as an optimized design for the mid-frequency range, owing to the presence of multiple bandgaps within this domain. These two configurations, along with their corresponding dispersion curves, are illustrated in Fig. 13.

Based on Fig. 13 showing the two optimal structures, the Sierpinski carpet structure with a square central rod has a total band gap of 3.09 kHz, while the Sierpinski carpet structure with a dodecagon central rod has a total band gap of 2.7 kHz.

The supercell structures of these two configurations are illustrated in Fig. 14.

Figure 14 shows the 8×8 supercell structures with square and dodecagonal central rods, where an acoustic source is placed at their center. Wave propagation in all directions has been analyzed both inside and outside the bandgap, and the results are presented in Figs. 15 and 16.

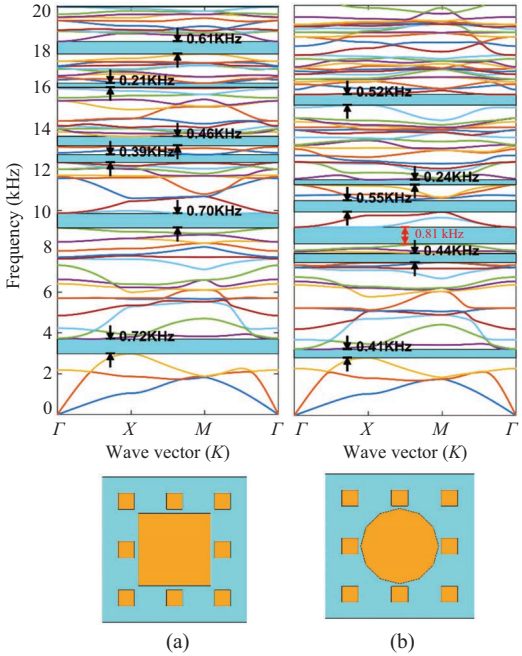


Fig. 13. Scattering curve of the unit cell of the Sierpinski carpet at $L = 2$ with a central rod: (a) square with a size of $a/2$ and (b) dodecagon.

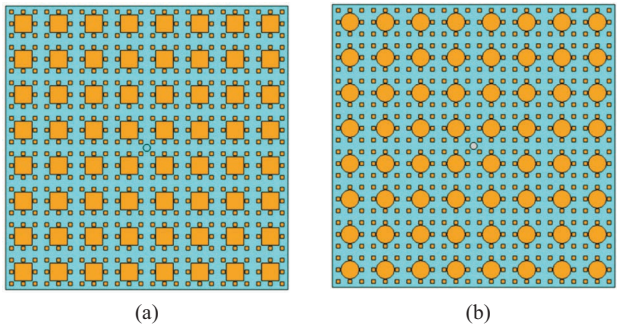


Fig. 14. The 8×8 supercell structure was designed with the central rods being (a) square and (b) dodecagonal.

According to Fig. 15(a), which shows the dispersion curve of the second-stage ($L = 2$) Sierpinski carpet structure with a square central rod, two frequencies inside the bandgap and two outside the bandgap are indicated with dashed lines. Wave propagation at 2 kHz and 5 kHz, shown in Figs. 15(b) and 15(d), occurs throughout the entire structure because they are outside the bandgap range. However, in Figs. 15(c) and 15(e), corresponding to frequencies of 3.5 kHz and 9.5 kHz, since they fall within the bandgap, the wave becomes localized at the center of the structure.

In Fig. 16(a), the dispersion curve of the second-stage Sierpinski carpet structure with a dodecagonal central rod is shown, where two frequencies inside the bandgap and two outside the bandgap are marked with dashed lines. Wave propagation at 2 kHz and 5 kHz, shown in Figs. 16(b) and 16(d), occurs throughout the entire structure because these frequencies

are outside the bandgap. However, in Figs. 16(c) and 16(e), corresponding to frequencies of 3 kHz and 8.5 kHz, the waves are within the bandgap range and thus become localized at the center of the structure.

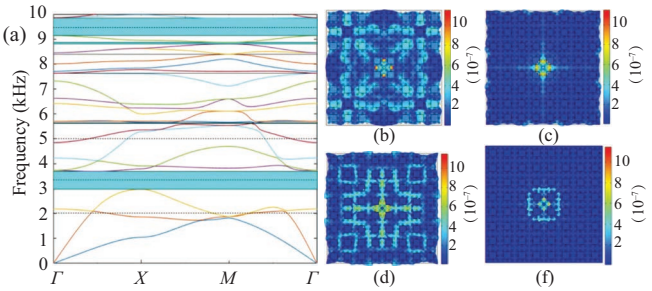


Fig. 15. (a) Dispersion curve of the unit cell with a square central rod. Wave propagation in the 8×8 supercell structure with square rods at frequencies (b) 2 kHz, (c) 3.5 kHz, (d) 5 kHz, and (e) 9.5 kHz.

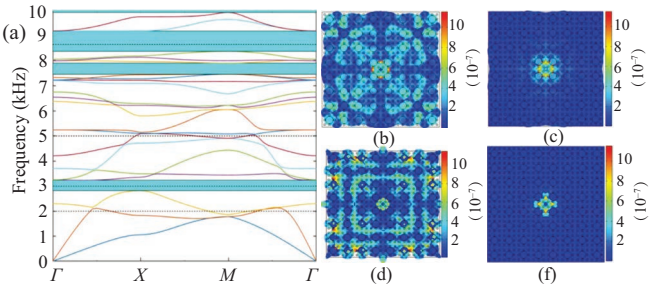


Fig. 16. (a) Dispersion curve of the unit cell with a square central rod. Wave propagation in the 8×8 supercell structure with dodecagonal rods at frequencies (b) 2 kHz, (c) 3 kHz, (d) 5 kHz, and (e) 8.5 kHz.

5. Conclusion

This study investigates the influence of various geometric parameters of rods on the phononic band gaps in structures based on the quasi-Sierpinski carpet. The results indicate that rod rotation, an increase in the central rod size, and other geometric modifications directly affect the location, number, and width of the band gap. The second-stage ($L = 2$) structures exhibited superior performance in generating band gaps at mid-range frequencies, while polygonal shapes such as dodecagons and hexadecagons produced the widest gaps at higher frequencies.

The proposed approach is scalable; the design principles can be applied to micro-scale devices such as MEMS resonators and acoustic filters, as well as macro-scale engineering systems including seismic dams and large-scale sound insulation. However, fabricating complex fractal geometries with high precision is challenging, and the results of this study are based on numerical simulations, so experimental validation is necessary to confirm actual performance.

The findings can serve as an effective strategy for the design and optimization of phononic crystals in engineering applications such as sound insulation, vibration control, and earthquake-resistant systems, and with further optimization and experimental testing, they can provide a foundation for scalable and tunable wave-control devices.

References

[1] Khelif A and Adibi A 2015 *Phononic Crystals* (Berlin: Springer) p. 978
[2] Dos Santos V G R C, de Miranda E J P Jr and Campos Dos Santos J M 2022 *International Symposium on Solid Mechanics* (Springer)
[3] Yang M, Ma G C, Wu Y, Yang Z Y and Sheng P 2014 *Phys. Rev. B* **89** 064309
[4] Huang J and Shi Z 2015 *J. Geotech. Geoenviron. Eng.* **141** 04015018
[5] Huang J, Lü C and Wu J 2017 *Smart Mater. Struct.* **26** 035061
[6] Xu Z X, Li Y, Zhang D, Zhang H G, Wang Y S and Chen W Q 2020 *Phys. Rev. Appl.* **14** 054016
[7] Bahrami A and Motaei F 2024 *Prog. Energy* **7** 012002
[8] Bahrami E and Bahrami A 2024 *Eur. Phys. J. Plus* **139** 609
[9] Huang J, Shi Z and Huang W 2017 *Physica B* **516** 48
[10] Oltulu O, Kaya A and Celik O 2022 *Period. Polytech. Electr. Eng. Comput. Sci.* **66** 169
[11] Huang J, Ruzzene M and Chen S 2017 *J. Sound Vib.* **395** 127
[12] Ozer Z, Ozturk A S, Sadigh H K, Solmaz M and Ozer R P 2020 *Eur. Phys. J. Appl. Phys.* **90** 20902
[13] Norris R C, Hamel J S and Nadeau P 2008 *J. Appl. Phys.* **103** 104908
[14] Wang K, Liu Y, Liang T and Wang B 2018 *J. Phys. Chem. Solids* **116** 367
[15] Liu X J and Fan Y H 2013 *Chin. Phys. B* **22** 036101
[16] Vasseur J O, Deymier P A, Chenni B, Lambin P, Laude D and Djafari-Rouhani B 2002 *Phys. Rev. E* **65** 056608
[17] Oltulu O, Mamedov A M and Ozbay E 2017 *Appl. Phys. A* **123** 212